

## RESEARCH ARTICLE

10.1002/2017JA024177

## Key Points:

- Study presents a newly coupled model capable of treating the superthermal electron population in the global polar wind solution
- Single stationary field line solutions under sunlit and dark conditions are presented as is the global solution from ~1000 moving lines
- Field line motion creates global structure by transporting field lines through different conditions of illumination and Joule heating

## Correspondence to:

A. Glocer,  
alex.glocer-1@nasa.gov

## Citation:

Glocer, A., G. Khazanov, and M. Liemohn (2017), Photoelectrons in the quiet polar wind, *J. Geophys. Res. Space Physics*, 122, 6708–6726, doi:10.1002/2017JA024177.

Received 21 MAR 2017

Accepted 25 MAY 2017

Accepted article online 7 JUN 2017

Published online 14 JUN 2017

## Photoelectrons in the quiet polar wind

A. Glocer<sup>1</sup> , G. Khazanov<sup>1</sup> , and M. Liemohn<sup>2</sup> 

<sup>1</sup>NASA/GSFC, Greenbelt, Maryland, USA, <sup>2</sup>Climate and Space Sciences and Engineering Department, University of Michigan, Ann Arbor, Michigan, USA

**Abstract** This study presents a newly coupled model capable of treating the superthermal electron population in the global polar wind solution. The model combines the hydrodynamic Polar Wind Outflow Model (PWOM) with the kinetic SuperThermal Electron Transport (STET) code. The resulting PWOM-STET coupled model is described and then used to investigate the role of photoelectrons in the polar wind. We present polar wind results along single stationary field lines under dayside and nightside conditions, as well as the global solution reconstructed from nearly 1000 moving field lines. The model results show significant day-night asymmetries in the polar wind solution owing to the higher ionization and photoelectron fluxes on the dayside compared to the nightside. Field line motion is found to modify this dependence and create global structure by transporting field lines through different conditions of illumination and through the localized effects of Joule heating.

## 1. Introduction

Much of the plasma in the magnetosphere is known to be of ionospheric origin. The significance of the ionospheric source of plasma is such that it has even been suggested to be fully sufficient to account for the majority of magnetospheric plasma [Chappell *et al.*, 1987]. This is especially true during geomagnetic storms where it has been demonstrated that O<sup>+</sup>, an indisputable indication of an ionospheric source, is found to be a major component [e.g., Lennartsson *et al.*, 1981]. The presence of ionospheric plasma affects all parts of the space environment such as the ring current [e.g., Shelley *et al.*, 1972], the reconnection rate [e.g., Shay *et al.*, 2004], and magnetospheric convection [e.g., Glocer *et al.*, 2009b] to name a few. It is therefore imperative to understand the processes involved in transporting ionospheric plasma to the magnetosphere.

Outflows of ionospheric plasma along open magnetic field lines was first suggested by Dessler and Michel [1966] and Nishida [1966]. Later the concept of a “polar wind” was introduced by Axford [1968] and Banks and Holzer [1968] to suggest that the outflow would become supersonic. They called this persistent outflow the polar wind as it is similar in concept to the solar wind. The polar wind concept was later confirmed observationally by the Explorer 31 and ISIS 2 satellites [Hoffman, 1970; Brinton *et al.*, 1971; Hoffman *et al.*, 1974]. Since that time, it has been shown that there are many contributing processes to ionospheric outflow. Detailing each of these processes is outside the scope of this paper, but we refer the interested reader to the reviews by Yau *et al.* [2007, and references therein] and Welling *et al.* [2016, and references therein]. In this paper, our primary focus is on the role of photoelectrons in the quiet time polar wind.

Photoelectrons are generated when solar EUV impinges on the neutral atmosphere creating ions and electrons. It was first suggested that these photoelectrons could affect the polar wind solution by Axford [1968] and Lemaire [1972]. Essentially, they suggested that the relatively energetic photoelectrons would try to separate from the more massive cold ion population giving rise to an enhanced electric field which would retard the escape of the electrons while simultaneously accelerating the ions. Photoelectrons can also influence the thermal plasma solution through energy deposition to the thermal electrons via Coulomb collisions [e.g., Yau *et al.*, 1995]. Observations generally support the idea that photoelectrons exert some influence on quiet time polar wind solution. For instance, Abe *et al.* [1993] showed that polar wind velocity is higher in the dayside polar cap than the nightside. As the photoelectron flux is observed to be greater at lower solar zenith angles (SZAs) than at higher SZA [Lee *et al.*, 1980; Peterson *et al.*, 2008], the day-night asymmetry in the observed velocity is suggestive of the importance of photoelectrons. Likewise, a statistical study of polar region observations of electron density by Akebono and electron and ion temperature observed by European Incoherent Scatter (EISCAT) Svalbard Radar (ESR) shows a strong SZA dependence [Kitamura *et al.*, 2011].

Subsequent modeling by *Glocer et al.* [2012] demonstrated that photoelectron effects are likely more responsible for this observed SZA dependence than enhanced ionization.

Given the importance of photoelectrons in understanding the quiet time polar wind solution, there have been several efforts to include them in numerical models. Modeling work by *Tam et al.* [1995] and *Tam et al.* [1998] demonstrated that photoelectrons can influence the  $O^+$  solution, although the predicted temperatures were higher than observed values. Simulations by *Khazanov et al.* [1997] showed a clear connection between the concentration of photoelectrons, relative to thermal electrons, and the ambipolar potential and polar wind solution. Modeling work by *Wilson et al.* [1997] and *Su et al.* [1998] have found similar results and further investigated the consequences of a high-altitude potential drop above three Earth radii. Such a potential drop is one way to satisfy the zero current condition which states that the photoelectron flux must be balanced by a combination of ion flux and thermal electron flux; a high-altitude potential drop would reflect a portion of the photoelectron population thereby reducing the net flux. *Varney et al.* [2014] examined this issue in great detail using a field-aligned polar wind simulation with kinetic electrons and fluid ions using different potential drop values. Their results suggest that increasing the value of the potential drop lowers the electron temperature at high altitudes and increases it at lower altitudes.

Currently missing in existing models of ionospheric outflow is a global approach including a fully kinetic treatment of the superthermal electrons. The previous works described above are either applied to stationary single flux tubes or are global but rely on externally imposed calculations of the superthermal electron population [e.g., *Glocer et al.*, 2012]. The purpose of the present work is to fill this gap by presenting a newly capable model combining a fully kinetic model of the superthermal electron population with a global hydrodynamic polar wind model. While our focus here is on the photoelectrons, the model can potentially include other superthermal populations as well. How the photoelectrons control the global structure of the quiet time polar wind and how ionospheric convection affects this solution are central questions addressed in this study.

In this paper we describe a newly coupled model combining the Polar Wind Outflow Model (PWOM) with the SuperThermal Electron Transport (STET) code. The coupled PWOM-STET code is capable of studying the role of photoelectrons on the global polar wind solution. We describe the models and their coupling in section 2. The results are presented in section 3 and cover steady state dayside and nightside conditions, global simulations including the effects of convection, and a cursory examination of the effect of including a reflection potential. We summarize our results and discuss our conclusions in section 4.

## 2. Model Details

Assessing the role of Superthermal Electrons (SE) in the formation of ionospheric outflow requires a global model capable of fully treating the thermal ions and electrons as well as the SE population. These populations should be modeled self-consistently such that the production of an SE is paired with the production of a corresponding ion, the energy loss of an SE due to Coulomb collisions with the thermal electron population is paired with a corresponding energy source for the thermal population, and the ion and electron populations are coupled together via the ambipolar electric field. We therefore couple two models, the Polar Wind Outflow Model (PWOM) and the SuperThermal Electron Transport (STET) code, in order to create a newly capable tool to study the role of superthermal electrons in the global polar wind solution. The following subsections detail each of the models and describe the coupling scheme.

### 2.1. The Polar Wind Outflow Model

The Polar Wind Outflow Model (PWOM) [*Glocer et al.*, 2007, 2009a, 2009b], based on the earlier polar wind model of *Gombosi et al.* [1985], is a global model of polar wind outflow. The model was recently described in detail by *Glocer et al.* [2009a] and *Glocer et al.* [2012], so only a summary of the model is provided here. PWOM determines the solution of ionospheric  $H^+$ ,  $O^+$ ,  $He^+$ , and electrons in the transition region between the magnetosphere and ionosphere, covering an altitude range from 250 km to 8000 km. The global polar wind solution is obtained by solving the field-aligned gyrotopical transport equations along several field lines as they convect around the high-latitude region. This gives a hydrodynamic solution for the ion populations. The neutral thermosphere is externally imposed by using the MSIS-90 (Mass Spectrometer and Incoherent Scatter) empirical model [*Hedin*, 1983, 1987, 1991]. Chemical sources and losses, collisional interactions, and Joule heating processes are all included.

Of particular importance to the present study is the inclusion of photoelectron dynamics. As described by *Glocer et al.* [2012], we split the electron population in to two pieces: thermal and superthermal. Unlike the ions, the electrons are not solved using the full transport equations. Instead, they are determined using conditions of quasi-neutrality,

$$n_e + n_\alpha = \sum_i n_i \quad (1)$$

the current conservation condition,

$$n_e u_e + n_\alpha u_\alpha = \left( \sum_i n_i u_i - \frac{j}{e} \right) \quad (2)$$

$$j = j_0 \frac{A_0}{A} \quad (3)$$

and an energy equation,

$$\rho_e \frac{\partial T_e}{\partial t} = (\gamma_e - 1) \frac{m_e}{kA} \frac{\partial}{\partial r} \left( A \kappa_e \frac{\partial T_e}{\partial r} \right) - \rho_e u_e \frac{\partial T_e}{\partial r} - T_e \left[ S_e + \frac{\gamma_e - 1}{A} \rho_e \frac{\partial}{\partial r} (A u_e) \right] + (\gamma_e - 1) \frac{m_e}{k} \frac{\delta E_e}{\delta t} \quad (4)$$

where  $n_e$  is the thermal electron density,  $n_\alpha$  is the density of superthermal electrons, and  $n_i$  is the density of ion species "i." Also, in equations (1)–(4),  $\rho_e$  is the thermal electron mass density,  $m_e$  is the mass of an electron,  $T_e$  is the electron temperature,  $A$  is the flux tube cross-sectional area,  $u_i$  is the bulk velocity of the  $i$ th ion species,  $u_e$  is the thermal electrons bulk velocity,  $u_\alpha$  is the superthermal electron bulk velocity,  $\delta E_e / \delta t$  is a source term that includes the collisional interactions,  $\gamma_e$  is the polytropic index,  $S_e$  is the thermal electron production term,  $\kappa_e$  is the electron heat conduction coefficient,  $r$  is the radial distance along the field line,  $j$  is the current density which is zero in this study but kept for completeness,  $k$  is Boltzmann's constant, and the subscript "0" represents the value taken at a reference altitude.

The ambipolar electric field ( $E_{\parallel}$ ) is determined from a generalized Ohm's law approach where the full electron momentum equation is considered in the steady state and then we solve for the  $E_{\parallel}$ . The resulting equation is given by [*Gombosi and Nagy, 1989*]

$$E_{\parallel} = -\frac{1}{en_e} \left[ \frac{\partial}{\partial r} (p_e + \rho_e u_e^2) + \frac{A'}{A} \rho_e u_e^2 \right] + \frac{1}{en_e} \frac{\partial}{\partial r} \left( \sum_i \frac{m_e}{m_i} \left[ (u_e - u_i) S_i - \frac{\delta M_i}{\delta t} \right] + \frac{\delta M_e}{\delta t} \right) \quad (5)$$

$m_i$  is the ion mass,  $S_i$  is the mass source rate, and  $\frac{\delta M}{\delta t}$  is the momentum exchange rate which is modified to now include the Coulomb collisional coupling between the thermal and superthermal components.  $p_e$  is the thermal electron pressure,  $e$  is the electron charge, and  $A'$  is the spatial derivative along the field of the cross-sectional area of the flux tube.

It is interesting to note that it is possible to obtain an expression for  $E_{\parallel}$  without assuming a steady state for the electrons as done by *Liemohn et al.* [1997]. They accomplished this by using the currentless condition (our equation (2) with no current) to replace the time derivative term in the electron momentum equation with time derivatives of the ion and superthermal electron mass flux. They then use the ion momentum equation to replace the resulting time derivative term of the ion mass flux. The end result is an equation very similar to our equation (5), but with a few additional terms related to the ion pressure gradient, ion inertia, and the time derivative of the superthermal electron mass flux. The ion pressure gradient and inertial terms are not expected to contribute much as they are multiplied by  $m_e/m_i$  which is a small number; these terms can therefore be safely neglected. It is possible that the time derivative of the superthermal electron mass flux could be an important contributor to the field; however, as discussed later, the time dependence of the superthermal electron solution is neglected for computational efficiency as the full time-dependent superthermal electron solution would be too demanding in a global calculation. Like a number of previous studies [e.g., *Varney et al., 2014*], we therefore do not consider this term either. As a result, equation (5) does not have the moments of the superthermal electrons represented explicitly. Nevertheless, as noted by *Varney et al.* [2014], their effects are included implicitly through their modification of the thermal electron density, velocity, and pressure.

As seen from the equations above, the effect of photoelectrons can be accounted for in the global polar wind solution by specifying the superthermal electron density and bulk velocity. We must also specify the ion production rate, which is paired with superthermal electron production, and the portion of the energy source term representing the transfer of energy from the superthermal electrons to the thermal electrons via

Coulomb collisions. In *Glocer et al.* [2012] the photoelectron parameters were set at the bottom of the model and mapped to higher altitudes to obtain the superthermal density and velocity. However, the ion production rate was not consistent with the photoelectron production, and the Coulomb collisional interaction between superthermal electrons and thermal electrons was neglected. In contrast, the present work uses the STET code, presented in the next section, to represent the complete kinetic superthermal electron solution. Note that STET uses the thermal electron density and electric field calculated by PWOM in its solution.

The boundary conditions and initial conditions for PWOM are set as follows. The ions at the lower boundary are assumed to be in chemical equilibrium with zero bulk velocity and a temperature equal to the neutral temperature. The upper boundary velocity and temperature are assumed to have zero derivative. The pressure is set to have a slight gradient to ensure that any plasma reaching the upper boundary is pulled out. The density can then be set accordingly by the ideal gas law. The electron temperature is set to match the ion and neutral temperature at the bottom of the simulation and is assumed to have zero derivative at the top of the simulation. For the initial condition, we take an initial guess of a steady state simulation from a prior run which then propagates out of the simulation over the course of several hours. For steady state runs, PWOM is run in a time dependent mode until the simulation result is no longer changing. For time dependent simulations, PWOM is first run to steady state, then the time is reset to zero and the time-dependent simulation proceeds from the steady state initial condition.

## 2.2. SuperThermal Electron Transport

The SuperThermal Electron Transport (STET) code has been successfully used in multiple studies to model the generation and transport of the hot electrons in the space environment [see, e.g., *Khazanov et al.*, 1994; *Khazanov and Liemohn*, 1995; *Liemohn and Khazanov*, 1995; *Khazanov et al.*, 2013]. Of particular relevance to this study is the form of the solution that includes the effect of the parallel electric field on the SE solution. This is because the parallel electric field is an essential part of the coupling of the SE population to the polar wind ion solution. Therefore, we adopt the approach presented in *Liemohn et al.* [1997] which modified STET to include the effect of the parallel electric field while minimizing numerical diffusion. We refer the reader to that paper for full details, but a brief summary of the approach is given in the remainder of this subsection.

The time-dependent evolution of the SE population along a magnetic field line is given by the solution of the Boltzmann-Landau equation. That equation can be averaged over the electron gyration in order to reduce the dimensionality of the problem. The result can be presented as [*Khazanov et al.*, 1994]:

$$\frac{\beta}{\sqrt{E}} \frac{\partial \phi}{\partial t} + \mu \frac{\partial \phi}{\partial s} - \frac{1 - \mu^2}{2} \left( -\frac{F}{E} + \frac{1}{B} \frac{\partial B}{\partial s} \right) \frac{\partial \phi}{\partial \mu} + EF\mu \frac{\partial}{\partial E} \left( \frac{\phi}{E} \right) = Q + \langle S \rangle \quad (6)$$

where  $\beta = 1.7 \times 10^{-8} \text{ eV}^{1/2} \text{ cm}^{-1} \text{ s}$ ,  $\phi = \phi(t, E, \mu, s)$  is the differential flux of SEs,  $E$  is the kinetic energy,  $\mu$  is the cosine of the local pitch angle,  $s$  is the distance along the field line,  $B$  is the magnetic field,  $F$  is the field-aligned force resulting from a parallel electric field,  $Q$  is production rate, and  $\langle S \rangle$  is the collision operators.

Solving equation (6) is replete with challenges. To obtain a numerical solution, we must first construct a grid to discretize the problem in  $E$ ,  $\mu$ , and  $s$ . Doing so, however, can lead to excessive numerical diffusion as particle trajectories are not aligned with the grid in this coordinate system. To understand this problem, consider a particle moving along the magnetic field with some  $\mu = \mu_1$  and  $E = E_1$  in the absence of collisions. As the particle moves from one position along the field line to another, the magnetic field changes which causes the pitch angle to change,  $\mu = \mu_2$ , in order to conserve the first adiabatic invariant. The presence of a parallel electric field further complicates this picture. If our example particle is moving along the field parallel to the electric field, the velocity will be retarded shifting the kinetic energy to lower and the pitch angle to larger values. Conversely, if the particle is moving the direction antiparallel to the electric field the velocity will increase, shifting the kinetic energy up and the pitch angle to more field-aligned values. Since  $E$  depends on the velocity, and  $\mu$  depends on the velocity and the magnetic field, particle trajectories will always be curved relative to a  $\mu$  and  $E$  grid. As described in the previous STET studies listed above, choosing to work in  $\mu$  and  $E$  coordinates can result in an overestimate of pitch angle scattering and particle trapping in the plasmasphere refilling problem.

It is therefore advantageous to consider a change of variables. Specifically, to work with the total energy ( $\epsilon$ ) instead of kinetic energy ( $E$ ), where  $\epsilon$  is determined by

$$\epsilon(s, E) = E - e\Delta\Phi(s) \quad (7)$$

where  $e$  is the electron charge and  $\Delta\Phi(s)$  is the electric potential difference relative to a reference altitude ( $\Delta\Phi(s) = \Phi(s) - \Phi_{\text{ref}}$ ). Likewise, we also work with the cosine of the pitch angle at a reference altitude ( $\mu_0$ ) instead of the cosine of the local pitch angle ( $\mu$ ), where  $\mu_0$  is given by

$$\mu_0(s, E, \mu) = \sqrt{1 - \frac{B_0 E}{B(s)[E - e(\Delta\Phi(s) - \Delta\Phi_0)]}(1 - \mu^2)} \quad (8)$$

where  $B(s)$  is the magnetic field at position  $s$  along the field line and the subscript “0” refers to the value at the reference altitude. Note that the reference altitude here is not necessarily the same as the reference altitude for the potential difference;  $\Delta\Phi_0$  is the potential difference between the two reference altitudes. Switching to these variables allows equation (6) to be presented in a much simpler form

$$\frac{\beta}{\sqrt{E}} \frac{\partial \phi'}{\partial t} + E\mu \frac{\partial}{\partial s} \left( \frac{\phi'}{E} \right) = Q' + \langle S' \rangle \quad (9)$$

where  $\phi' = \phi'(\epsilon, \mu_0, s)$  is the differential flux of SEs,  $Q'$  is the production rate, and  $\langle S' \rangle$  is the collision operators in the new variables. In this form, there are now no derivatives with respect to energy or pitch angle and particle trajectories are precisely aligned with the  $\epsilon - \mu_0$  grid. Therefore, transport described by the left-hand side of equation (9) does not result in any artificial numerical pitch angle scattering, and the only scattering that can occur is a result of the physical terms on the right hand side of the equation.

While equation (9) includes time dependence, it is often impractical to include this in our simulations owing to the intensive computational requirements. Therefore, we take advantage of the fact that the electrons respond much more quickly than comparatively heavier ions and assume that solving this equation in the steady state is sufficient. Note that this exact same assumption is made in determining the electric field as equation (5) is derived by taking the electron momentum equation in the steady state and solving for  $E_{\parallel}$ . Thus, every time that PWOM calls STET to get an updated solution for the superthermal electrons, STET starts with initially no superthermal electrons, calculates the sources, losses, and transport and returns back the steady state solution.

Working in  $\epsilon$  and  $\mu_0$  coordinates also enables us to better visualize possible particle trajectories in the SE solution. As an example, we consider an open magnetic field line with a 5 V potential drop from the ionosphere to the top of the simulation domain. Figure 1 shows the simulation grid in this scenario for three values of  $\epsilon$  that correspond to a value much greater, just above, and much less than the potential drop:  $\epsilon = 90$  eV (left), 6 eV (middle), and 2 eV (right). When the total energy is much greater than the potential drop, there are two types of particle trajectories (in the absence of collisions). These are the “fly through” trajectories in which electron remain in the loss cone as they fly from the ionosphere to the top of the simulation domain or from the top of the simulation domain to precipitate into the ionosphere (green), and the mirrored trajectories where electrons precipitate but are reflected back by magnetic mirroring before reaching the ionosphere (blue). When the total energy approaches, but is still greater than, the total potential drop, a new trapped trajectory becomes visible. This trapped trajectory represents particles that are trapped between mirror points entirely on one side of the equator (orange). Recall that mirror points are defined by when the local pitch angle reaches  $90^\circ$ , forcing the particle to change direction. These locations are defined by the spatial variation of the magnetic and electric fields. Finally, for total energies less than the total potential drop, the fly through trajectories are reflected such that the electrons are turned around before reaching the top of the simulations domain, and there exists a trapped trajectory with particles mirroring above the top of the ionosphere and being reflected before they reach the equator.

The creation of such “trapped zone islands” along a field line, represented by the orange trajectories in Figure 1, depends on the relationship of the magnetic field and the parallel electric potential difference as a function of distance along the field line. Specifically, if the field line dependence of  $B$  and  $\Phi$  satisfy these two equations [Chiu and Schulz, 1978; Khazanov et al., 1998],

$$\frac{d\Phi}{dB} > 0 \quad (10)$$

$$\frac{d^2\Phi}{dB^2} \leq 0 \quad (11)$$

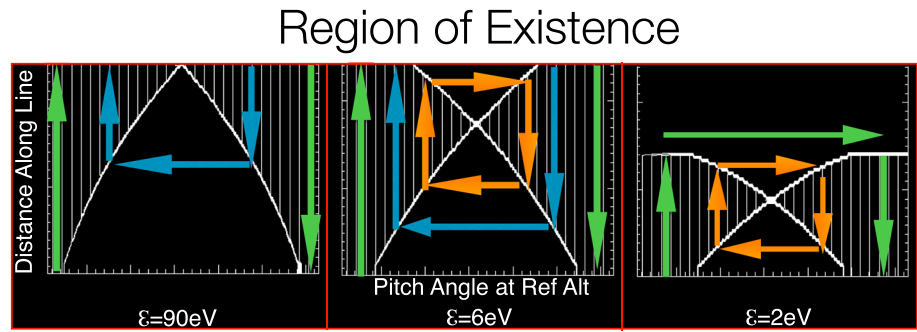


**Figure 1.** The region of existence for electrons with total energy of 90, 6, and 2 eV for the case of an open field line with a uniformly distributed 5 V potential drop from the top of the ionosphere to the top of the simulation domain. The horizontal axis represents the pitch angle at a reference altitude, and the vertical axis represents the distance along the field line; the top of the vertical axis top of the computational domain, and the bottom is the ionosphere. The arrows illustrate particle trajectories.

then no trapped zone islands will form along the field line. If either of these equations are violated, however, then one or more trapped zone islands will exist along the field line. *Chiu and Schulz* [1978] originally derived these formulas as a constraint on the famous *Knight* [1972] current-voltage relationship. *Liemohn and Khazanov* [1998] further developed this idea into a generalized current-voltage relationship that takes into account an arbitrary potential difference along the field line. *Khazanov et al.* [1998] continued the analysis for several specific scenarios of magnetospheric particle precipitation and polar wind outflow. The STET model can handle the formation of multiple trapped zones along the field line, down to the resolution of the  $s - \mu_0$  grid.

### 3. Results

We now present results from the newly coupled PWOM-STET code. These results are divided into three parts. First, we will consider a single, stationary, field line under sunlit and dark conditions. Then we examine the global outflow solution by following approximately 900 convecting field lines. The case with and without the effect of Joule heating is considered. Finally, we conduct a cursory examination of the impact of a high-altitude potential difference.

#### 3.1. Steady State Polar Wind Solution: Sunlit and Dark Conditions

The first part of our study focuses on the difference between the sunlit and dark steady state polar wind solutions. We consider two field lines, one in sunlight with a solar zenith angle (SZA) of 72°, and one in darkness

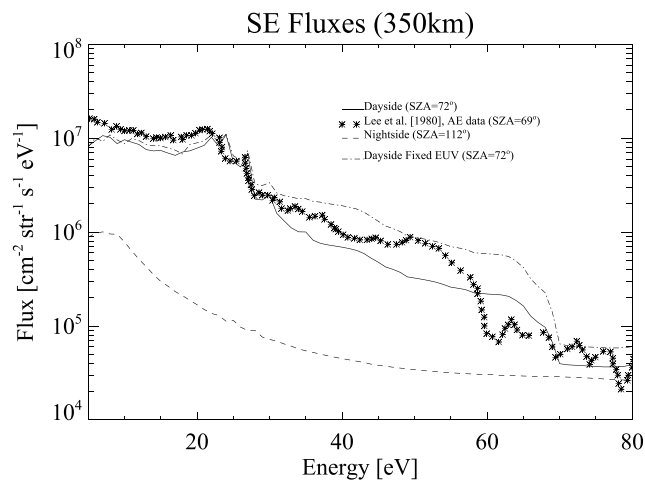


**Figure 2.** Photoelectron fluxes at 350 km altitude on the dayside (solid) and nightside (dashed). For reference, *AE* observations under similar illumination conditions are included (asterisk) from *Lee et al.* [1980]. Dayside fluxes with the EUV fluxes (below 25 nm) multiplied by a factor of 3 are shown with the dash-dotted line.

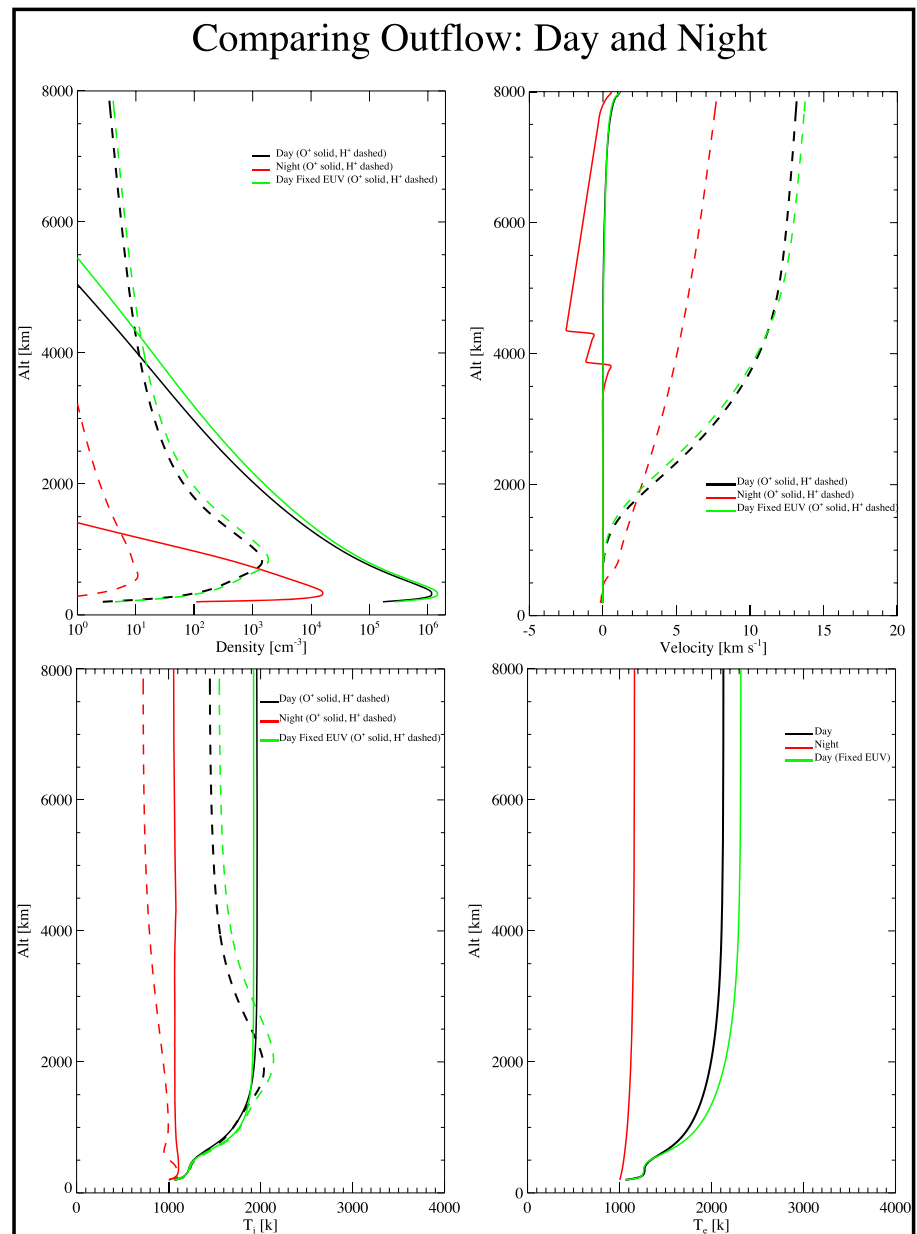


**Figure 3.** Comparison of the daytime (black) and nighttime (red) polar wind solution. Altitude profiles of O<sup>+</sup> (solid) and H<sup>+</sup> (dashed) density, velocity, and temperature are shown along with the electron temperature. Daytime polar wind solutions with the EUV fluxes (below 25 nm) multiplied by a factor of 3 are shown in green.

with a SZA of 112°. For sunlit conditions, the ionizing solar flux is determined by the incoming EUV and X-ray flux taken from the model of *Hinteregger et al.* [1981] and attenuated by the atmosphere. We assume an  $F_{10.7}$  of 180 corresponding to solar maximum conditions. For dark conditions, there is little or no direct solar flux, but light from both starlight and multiple resonant scattering is included. For the former, we adopt the approach described by *Titheridge* [2000] who estimated the incoming starlight intensity in three wavelength bands. For the later, we digitized the resonant scattering solution presented by *Strobel et al.* [1974] and interpolate the intensity at three wavelengths (LyAlpha, LyBeta, Hel, and Hell) to our particular SZA and altitude location on the field line. Each line is held in a fixed location, and the time-dependent simulation is run until a steady state solution is obtained. The energy grid spacing in the STET simulations is assumed to be 1 eV.

Figure 2 presents the simulated dayside and nightside SE fluxes as a function of energy. We focus on 350 km altitude as it allows us to directly compare the simulated SE fluxes with published AE observations with similar

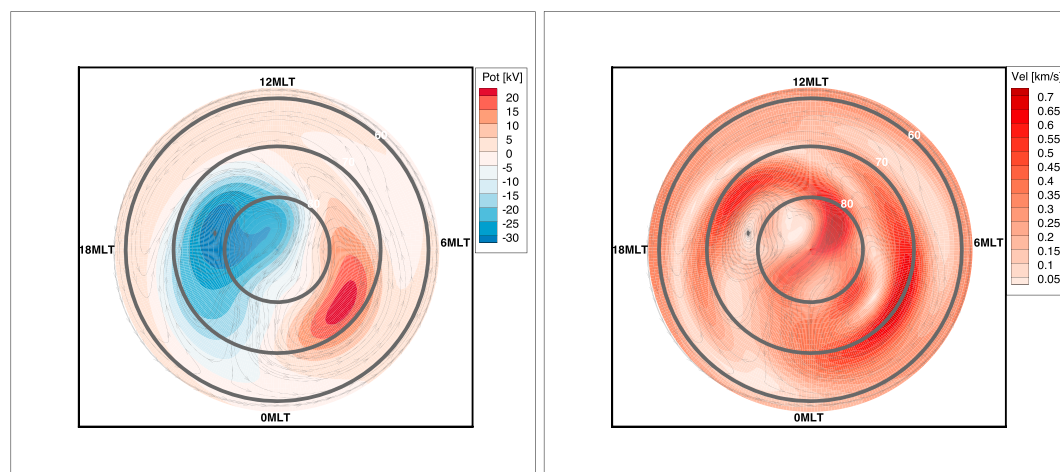


**Figure 4.** (left) Polar cap potential pattern used in calculation and (right) combined convection and corotation velocities. Streamlines are overlotted.

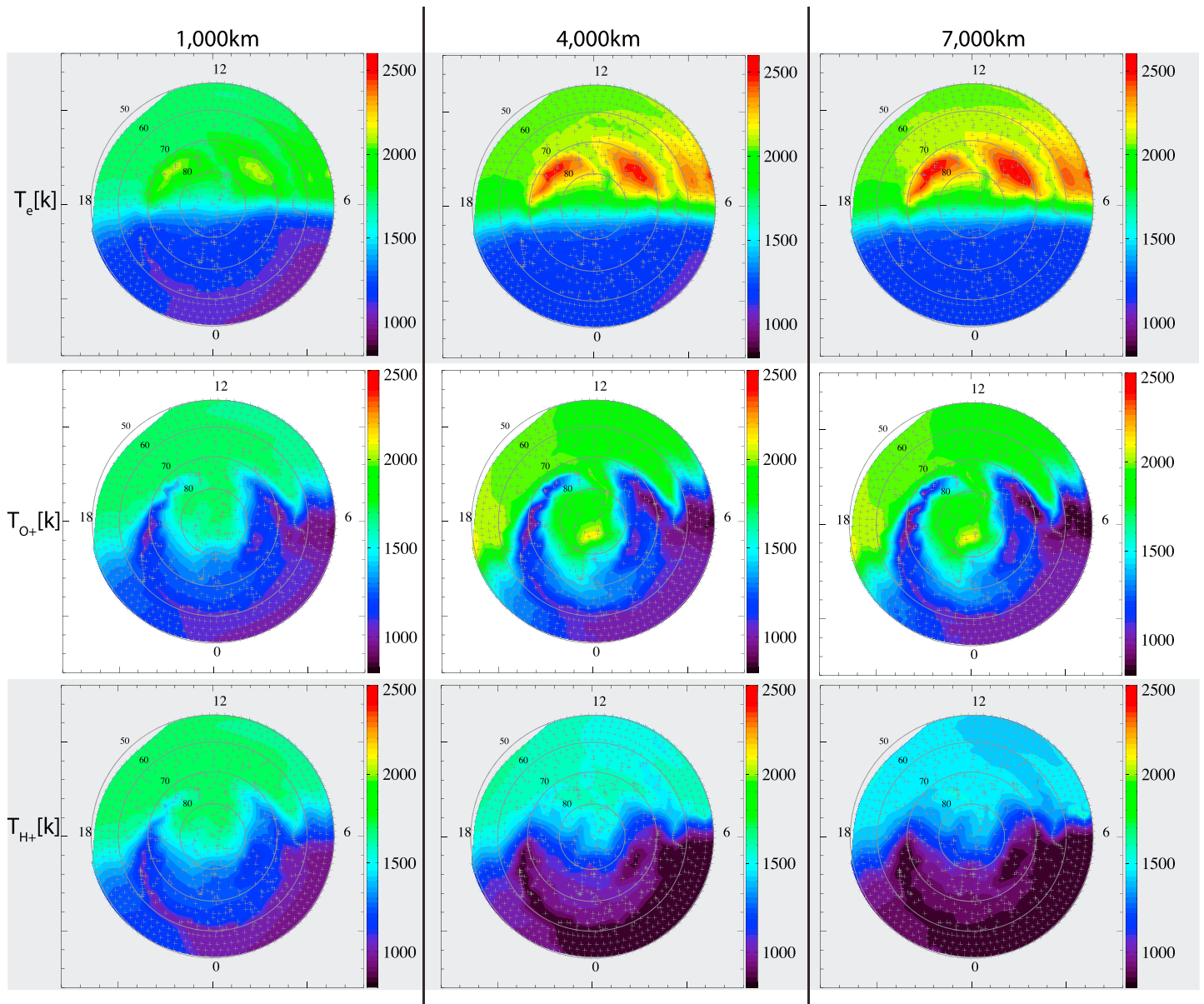
illumination conditions. It is not expected that the model will produce an exact match to the data, but the overall similarity of the observed and simulated spectra demonstrate that the model adequately represents the SE solution. We do not have a similar comparison of the nightside SE fluxes, but it is clear that the nightside fluxes are significantly lower than the dayside fluxes, as expected.

Figure 3 compares the day (black) and night (red) polar wind solutions calculated self-consistently with the SE fluxes discussed in the previous paragraph. This is the result of simulations of a stationary field line run in a time accurate mode until a steady state is reached. The figure presents the thermal plasma solution with densities in the upper left, velocities in the upper right, ion temperatures in the lower left, and electron temperature in the lower right. For the ion moments,  $O^+$  is shown in solid lines and  $H^+$  is shown in dashed lines. When examining the ion densities we find that, as expected, the dayside  $O^+$  and  $H^+$  densities are higher than on the nightside. Moreover, on the dayside the crossover altitude, where the simulation goes from an  $O^+$  dominated solution to an  $H^+$  dominated solution, changes from 4000 km to 1800 km.

From an observational point of view it is not known exactly where the crossover altitude is located, but statistical studies provide some expectation. *Chandler et al.* [1991] present DE-1 observations in the open field line region at invariant latitudes greater than  $70^\circ$  and altitudes between 1000 km and 4000 km. While that study did not look at the solar zenith angle dependence,  $O^+$  is found to dominate below 4000 km indicating the transition altitude should be above that altitude. Our crossover altitude prediction is therefore roughly consistent with observational expectations.

It is furthermore interesting to compare our simulation results which include a more comprehensive treatment of photoelectrons with the more simplified treatment using an externally imposed photoelectron population given by *Glocer et al.* [2012]. Both calculations show very low  $O^+$  velocity but significant day-night asymmetry in the  $H^+$  velocity. However, the size of the asymmetry is more pronounced in our current simulations. The peak  $H^+$  velocity is about 13.5 km/s under sunlit condition and 8 km/s under dark conditions for our simulations compared to 17 km/s and 13 km/s respectively in *Glocer et al.* [2012]. For reference, *Abe et al.* [2004] present average sunlit and dark  $H^+$  velocity values that peak at about 8 km/s and 5 km/s, respectively. Therefore, our new simulations more closely predict the  $H^+$  velocity but still overshoot the observed values. Both our new simulations and the prior simulations give reasonable predictions of the  $O^+$  velocities. The peak electron temperature is also predicted to be lower in our new simulations,  $T_e = 2200$  K, as compared to the calculation of *Glocer et al.* [2012],  $T_e = 4800$  K. Interestingly, the statistical value from EISCAT Svalbard Radar (ESR) determined by *Kitamura et al.* [2011],  $T_e = 3000$  K, is between these two values. Without a more comprehensive comparison it is impossible to say that the present results compare better with observations than the prior results of *Glocer et al.* [2012], but our initial look suggests the comparison to observations is reasonable. More importantly, the present coupled model achieves these results without having to rely on an external specification of the photoelectrons which is disconnected from the ion production.





**Figure 5.**  $T_e$ ,  $T_{O^+}$ , and  $T_{H^+}$  solutions at constant altitudes (1000, 4000, and 7000 km) in SM coordinates with MLT = 12 at the top of each plot. The latitudes represent invariant latitude. Each gray cross symbol represents the foot point location of one of the approximately 900 field lines tracked in the calculation.

One caveat to the present work is that the incoming EUV and X-ray flux is taken from the relatively dated model of *Hinteregger et al.* [1981]. *Richards et al.* [2006], as well as earlier studies [see, e.g., *Solomon et al.*, 2001, and references therein], indicated that the flux from this model below 25 nm wavelength needs to be adjusted upward by a factor of 2–3. To test the potential impact of this correction, we repeat our dayside simulation increasing the flux in this range by a factor of 3. The resulting SE fluxes are shown in Figure 2 as a dash-dotted line, and the associated polar wind solution is shown as green solid and dashed lines in Figure 3. This correction to the incoming solar flux serves to increase the SE fluxes with most of the effect visible above about 30 eV. The resulting thermal electron temperature is increased by a few hundred kelvins, or approximately 10%. The  $O^+$  and  $H^+$  densities are likewise increased slightly with the crossover altitude moving up a few hundred kilometers. This test demonstrates that while future work should incorporate a more recent model for the incoming solar flux, the expected difference in the polar wind solution will be fairly modest, and therefore, the older model of *Hinteregger et al.* [1981] is sufficient for the present study.

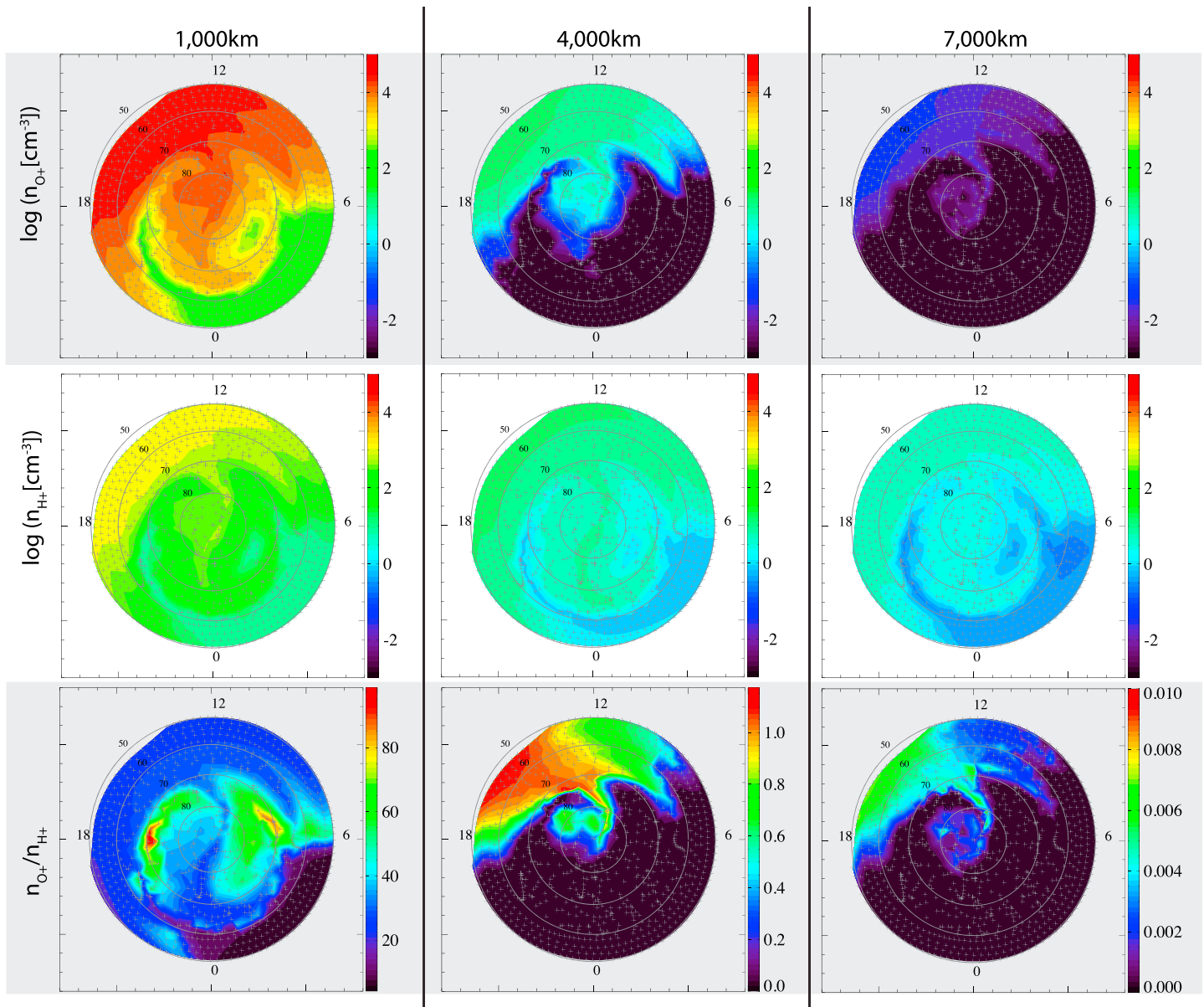


Figure 6. Same format as Figure 5 but plotting the log of  $n_{O^+}$  and  $n_{H^+}$  as well as  $n_{O^+}/n_{H^+}$ .

### 3.2. The Global Polar Wind Solution

The results shown in section 3.1 are illustrative of the steady state solution under typical steady sunlit and dark conditions but are missing the time dependent effects of field line convection. To address the effects of convection and examine the global polar wind solution in response to photoelectrons under position-dependent conditions of illumination, we simulate approximately 900 field lines distributed around and throughout the high-latitude region. Each line moving through the domain represents a field-aligned, coupled, PWOM-STET solution and all lines are combined to reconstruct the three dimensional result. Our initial condition is determined by holding the field lines stationary and obtaining a steady state solution for each field line. We then let the field lines move and track the time-dependent result. The simulation is run for 4 h after which the simulation settles into a quasi steady state.

The field lines in the simulations move under the combined influence of the convection and corotation velocities. The polar cap potential used to get the convection velocity in this study is specified by the empirical model of *Weimer* [2005] in response to nominal solar wind conditions assuming an IMF consistent with the Parker spiral. Specifically, the solar wind conditions and IMF conditions are held constant with a density

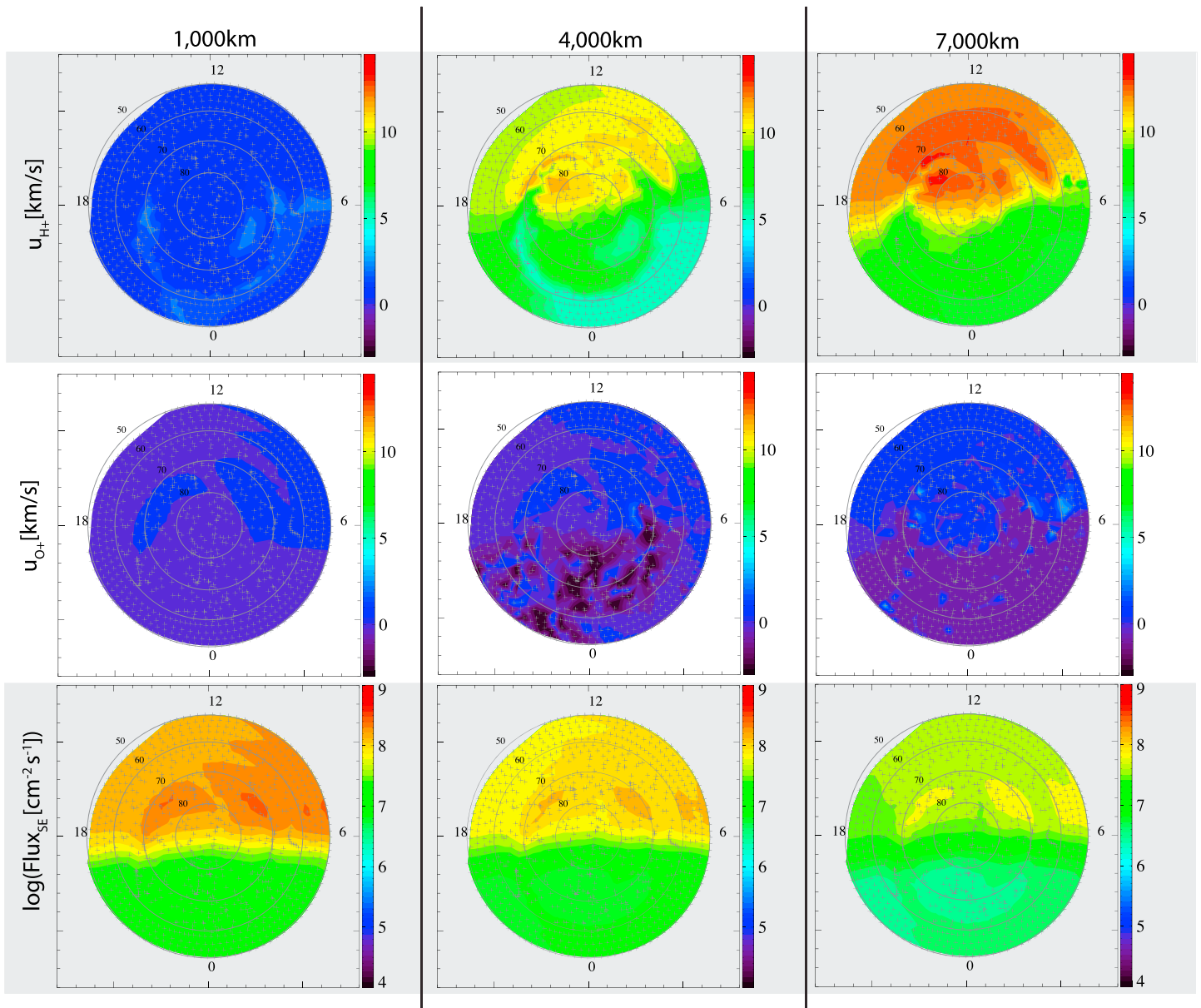
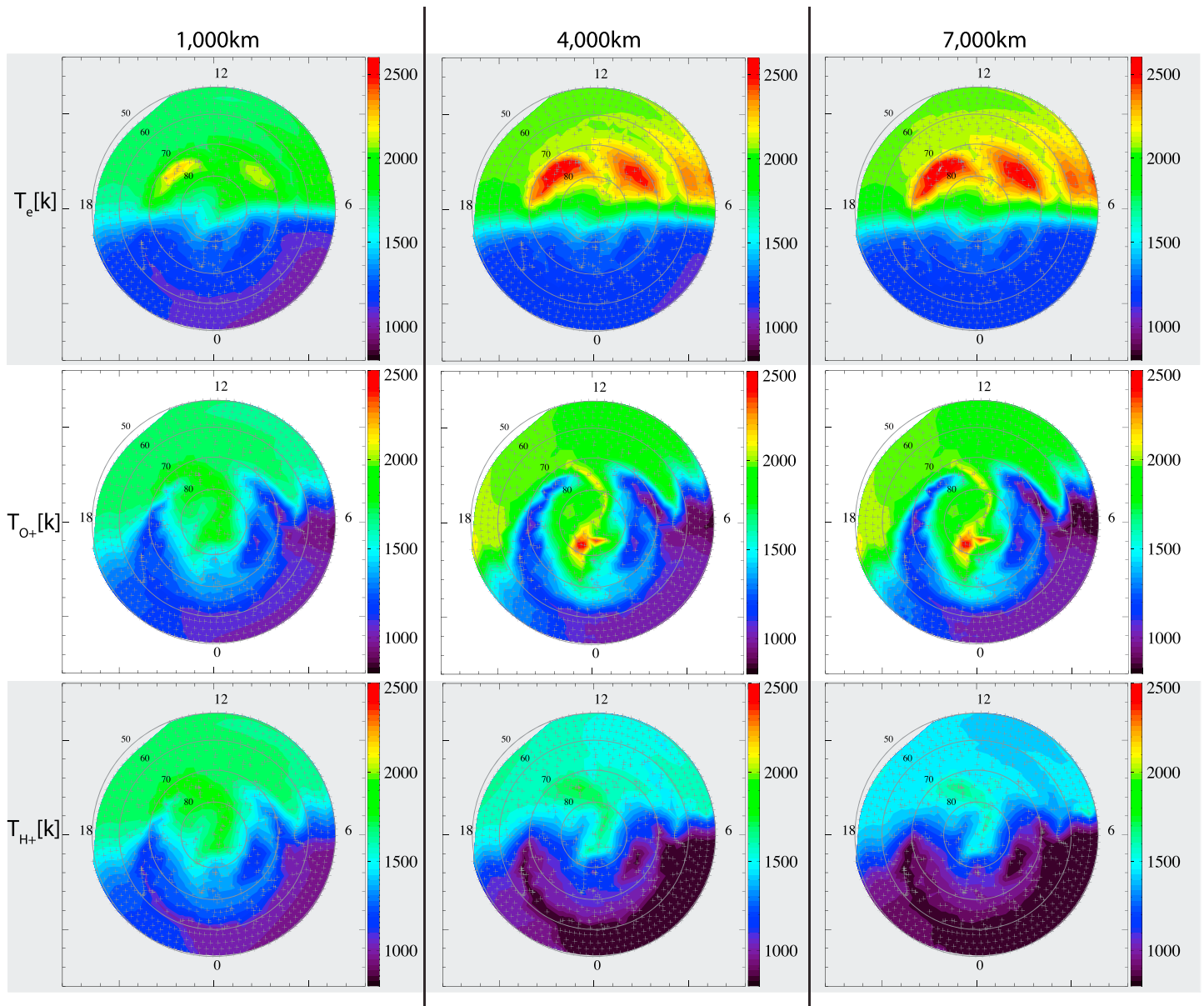


Figure 7. Same format as Figure 5 but plotting the log of  $u_{H^+}$  and  $u_{O^+}$ .

and velocity equal to  $5 \text{ cm}^{-3}$  and  $400 \text{ km/s}$  respectively, and  $B_x = B_y = 1 \text{ nT}$  and  $B_z = -1 \text{ nT}$ . When the model is coupled with the Space Weather Modeling Framework (SWMF), the polar cap potential is derived from the ionospheric electrodynamics component, a height integrated potential solver that combines ionospheric conductances with field-aligned currents calculated from Block-Adaptive-Tree Solar wind Roe-type Upwind Scheme (BATS-R-US) [Glocer et al., 2009a]. The convection electric field and the associated velocity is calculated from the potential; the field lines then move in response to convection. Figure 4 presents the polar cap potential and combined convection and corotation velocities used in this study.

The global polar wind solution including convection is shown in Figures 5–7. This solution includes the effects of time and position-dependent change of illumination and neutral background but neglects the effects of Joule heating which is considered later. Each row in these figures shows a color contour of a different physical quantity at three fixed altitudes (1000 km, 4000 km, and 7000 km) from the perspective of looking down on the high-latitude region from above. The gray crosses show the field line foot point locations, and the gray circles shows the invariant latitude. Magnetic local time (MLT) is indicated on the plot with 12 MLT at the top



**Figure 8.** Including effects of Joule heating.  $T_{e^-}$ ,  $T_{O^+}$ , and  $T_{H^+}$  solutions at constant altitudes (1000, 4000, and 7000 km) in SM coordinates with MLT = 12 at the top of each plot. The latitudes represent invariant latitude. Each gray cross symbol represents the foot point location of one of the approximately 900 field lines tracked in the calculation.

of each plot. Figure 5 presents the ion and electron temperatures, Figure 6 presents the ion densities and density ratios, and Figure 7 presents the ion velocities and the net photoelectron number flux.

In examining the global polar wind solution it is clear that there is a solar zenith angle dependence that is modified by the effects of convection. The relative importance of convection clearly depends on the mass of the species. For example, the electron temperature drops very quickly across the terminator, but the ion temperatures are slower to respond. The  $H^+$  temperature does transition to the nightside values more quickly than the  $O^+$  temperature, but both are slower to respond to changing illumination conditions than the electrons. This disparate response to changing illumination conditions can create some interesting localized feature. For instance, a region of higher ion temperatures along the “tongue of ionization” formed by the region of strong convection across the high-latitude region. Another such feature is localized enhancements of the electron temperature on the dayside between  $70^\circ$  and  $80^\circ$ . This localized enhancement appears in the region where flow is returning from the nightside to the dayside. The electrons are able to respond much more quickly

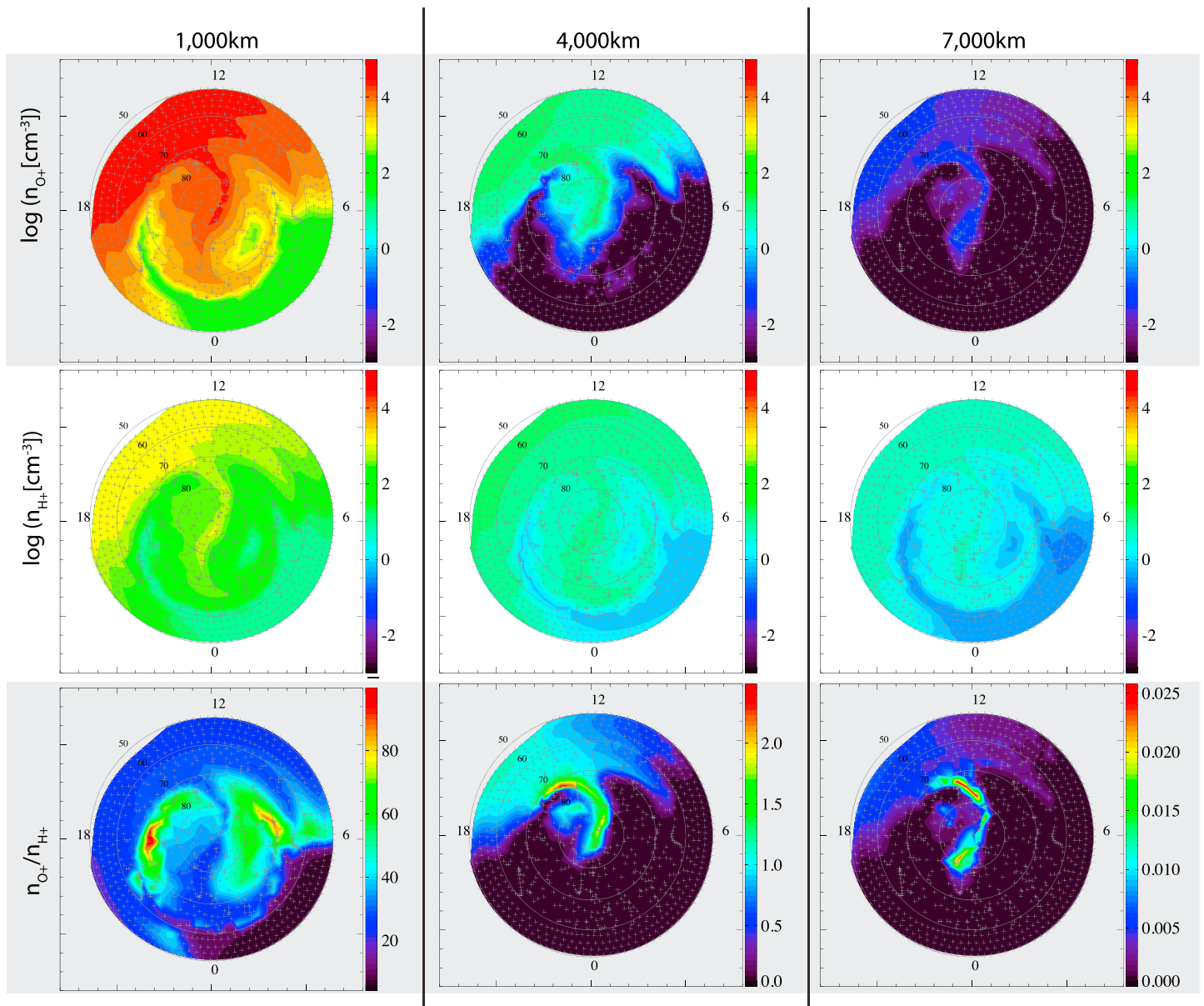


**Figure 9.** Same format as Figure 8 but plotting the log of  $n_{O^+}$  and  $n_{H^+}$  as well as  $n_{O^+}/n_{H^+}$ . Including effects of Joule heating.

to the sudden change in conditions, and they heat up while the ions persist at values closer to nightside conditions for longer. It is also interesting to note that the distribution of the electron temperature in polar region is closely tied to the distribution of the net number flux of photoelectrons. This is expected as there is no imposed topside heat flux, and therefore, the photoelectrons should exert the main influence in defining the thermal structure of the electrons.

The composition and velocity also exhibit strong SZA and altitude dependence modified by the effects of convection. Both  $O^+$  and  $H^+$  densities are enhanced on the dayside and drop off on the nightside, but both are enhanced along the region of enhanced convection dragging plasma across the high-latitude region. We also see that at higher altitudes the  $O^+$  to  $H^+$  ratio is enhanced on the dayside and drops precipitously on the nightside. Interestingly, there is an enhancement in the density ratio at low altitudes coinciding with the return flow. Just as in the single stationary field line case of Figure 3, both  $O^+$  and  $H^+$  ions have higher velocities under sunlit conditions as compared to dark conditions.

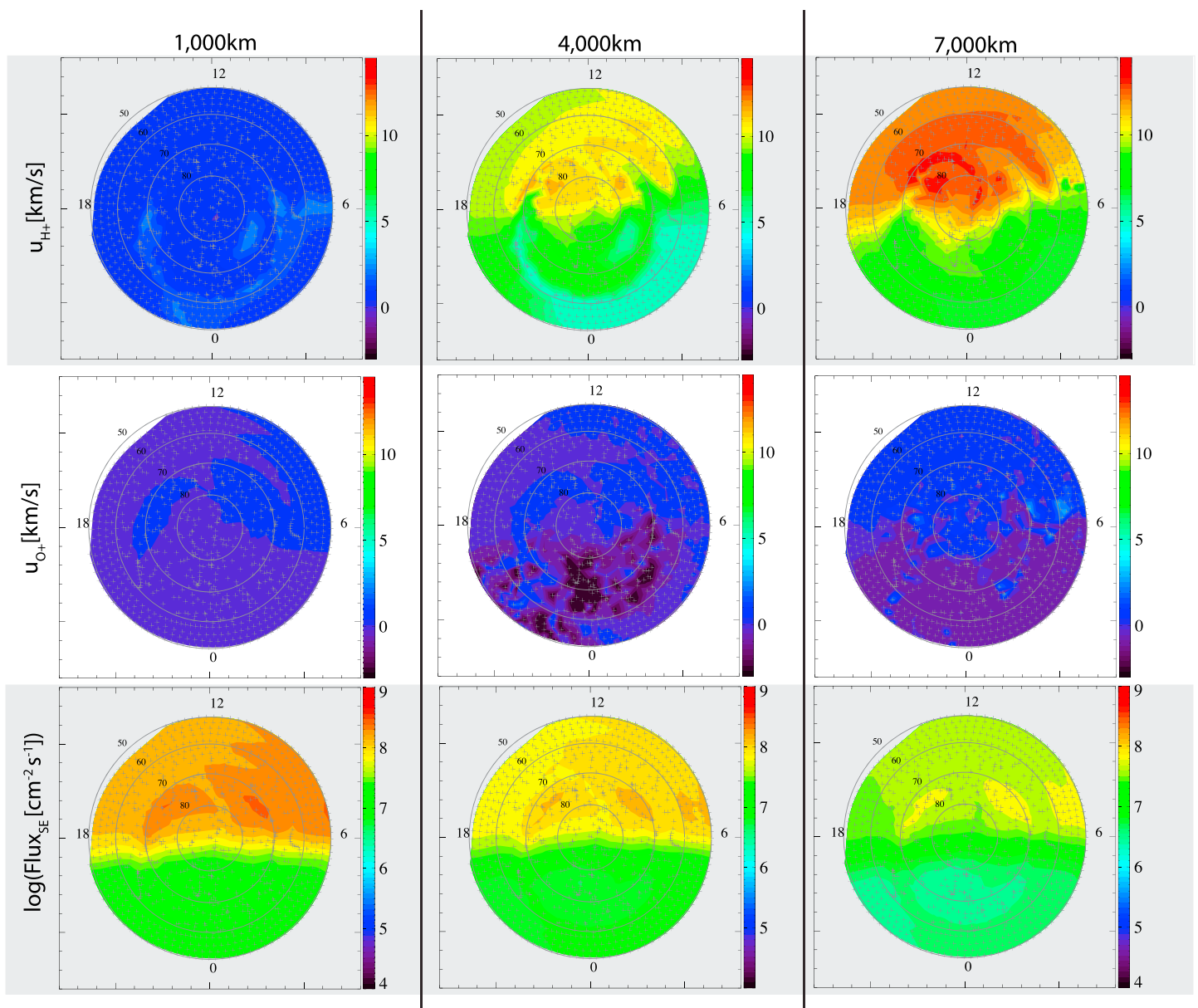


**Figure 10.** Same format as Figure 8 but plotting the log of  $u_{H^+}$  and  $u_{O^+}$ . Including effects of Joule heating.

The results just presented illustrate the nature of the global polar wind solution when convection is included but do not include the effects of Joule heating, low-altitude frictional heating, caused by the ions being “dragged” through the neutral background. Past studies indicate that this may have a significant effect of ion upwelling. For instance, *Cannata et al.* [1988] demonstrated that this frictional heating deposits energy below 500 km but can lead to transient upflow events. We now examine this effect on the global polar wind solution by including frictional heating associated with the perpendicular drift of ions through the neutral atmosphere. One simplification that is important to note is that we assume the neutrals are a static background and the ions are moving through them. In general, the neutral winds should be accounted for through either an empirical wind model such as that presented by *Hedin* [1991] and *Drob et al.* [2008], or a physics-based model. However, our simulations with a static neutral background suffice to demonstrate the basic effect.

The global polar wind solution including the effects of Joule heating are shown in Figures 8–10. These figures are presented in the same format as Figures 5–7 which do not include the Joule heating, but the color bars are somewhat different to accommodate the different range of values in the plots. Overall, the solution is much the same as when the additional heating is not included, but there are some localized differences. For instance

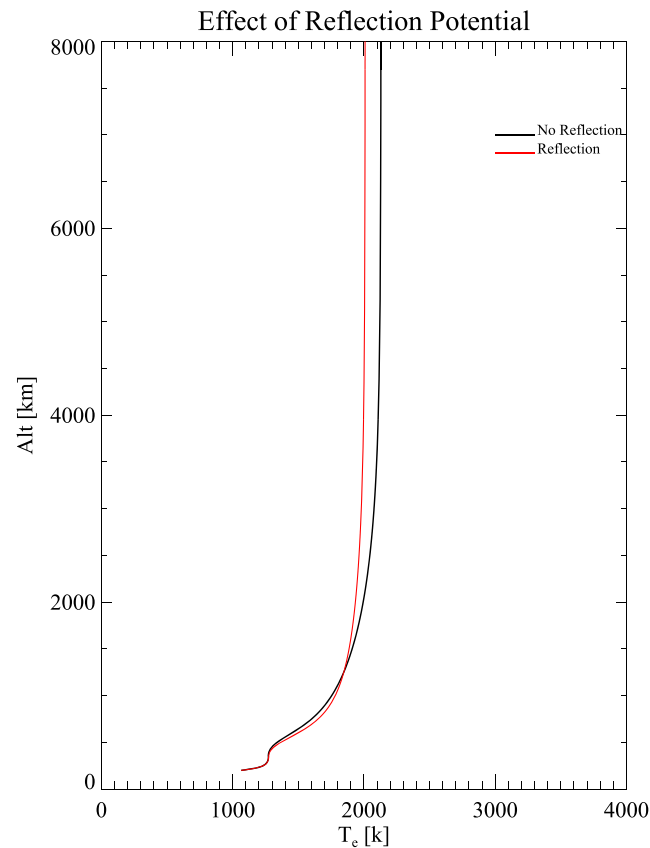


**Figure 11.** Altitude profile of the electron temperature with (red) and without (black) an imposed reflection potential.

the temperatures are enhanced along the region of strong convection on the dayside. This is particularly pronounced for the ions, but there is also some enhancement in the electron temperature. The densities at all altitudes also increase somewhat in the region of strong convection, with there being a higher  $O^+$  to  $H^+$  ratio in that region at 400 km. This supports the notion that the heating associated with convection can create localized enhancements of  $O^+$  at higher altitudes available for further acceleration by other processes.

### 3.3. A Cursory Examination of the Effect of Reflection Potential

Finally, we briefly address the sensitivity of the solution to the presences of a high-altitude reflection potential. It has been observed that a potential drop often exists at high altitudes. *Kitamura et al.* [2012] conducted a statistical study of 1 month of FAST data and found an average potential drop of about 20 V above 4000 km. This potential drop is referred to as a “reflection potential” since its presence is inferred by the observation of reflected photoelectrons whose kinetic energy is insufficient to overcome the electrical potential drop. While we do not model the high altitude potential drop above our simulation domain, in this subsection we conduct a cursory examination of the effect of an imposed reflection potential.

*Kitamura et al.* [2015] argued that the presence of a 20 V potential drop would choke off the photoelectron flux and since the flux of superthermal electrons must approximately equal the flux of ions, the polar wind would be suppressed as well. While it is true that one way to satisfy the current conservation condition implied by equation (2) is to require that the ion flux equal the photoelectron flux, that is not the only way to satisfy this condition. Indeed, thermal electrons are much more mobile and respond much more quickly than the ions. More generally, *Wilson et al.* [1998] describe three ways that the polar wind solution can respond to the flow of photoelectrons. First, thermal electrons can be drawn down the field line from the magnetosphere to counter the flow. Second, there could be a field-aligned current to counter the flow. Finally, a potential drop can form to reduce the flux of photoelectrons. It is this last scenario which we evaluate here.

To test the effect of the presence of a high-altitude potential drop we consider a single field line under sunlit conditions with a 20 V drop imposed just above the upper boundary of the model. We apply this potential

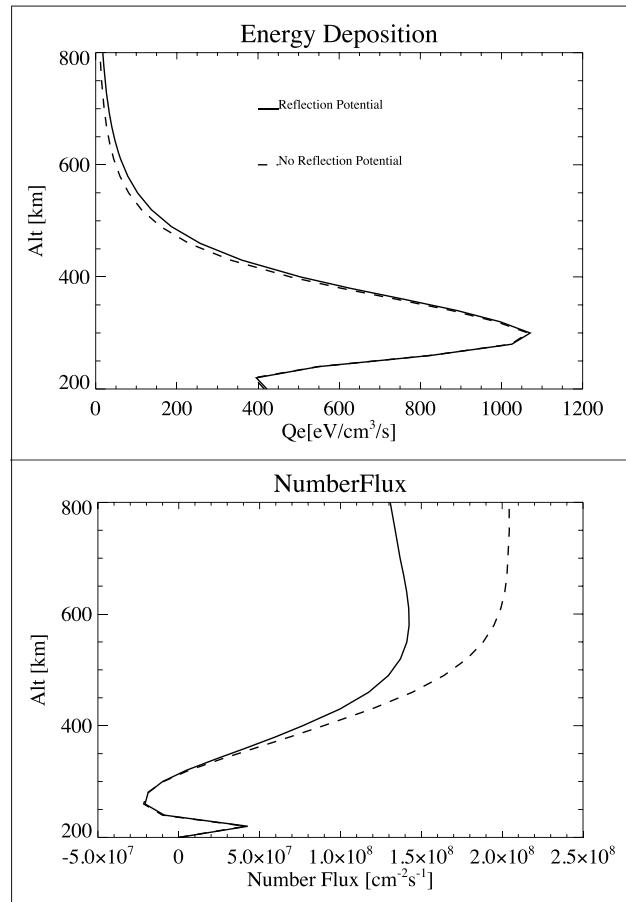


**Figure 12.** Altitude profile of the (top) superthermal electron energy deposition to the thermal plasma, and the (bottom) net number flux of superthermal electrons.

by setting downward flowing superthermal electrons with kinetic energy below 20 eV to match the upward flowing superthermal electrons with the same energy and pitch angle. While the potential drop at high altitudes above our simulation domain will also locally accelerate ions at those altitudes, we ignore that portion of the feedback on our simulation domain. Neglecting this is not expected to matter significantly as there is very little  $O^+$  at high altitudes to be further accelerated and the  $H^+$  is already supersonic when it reaches the upper boundary, and therefore, all of the characteristics point out of the simulation domain. Thus, the reflection of the upward flowing superthermal electrons is the main channel by which the potential drop is likely to affect our simulation domain.

In general, very little effect is found on the polar wind solution due to the presence of a reflection potential. In the interest of space we do not show all quantities but show only the electron temperature in Figure 11 as an example. At high altitudes the temperature is slightly lower while at lower altitudes the temperature is slightly higher. This is qualitatively similar to the results from Varney *et al.* [2014] who conducted a similar experiment imposing a potential drop at high altitudes and comparing the results with the RISR data.

It is instructive to also examine the effect that this reflection potential has on the superthermal electron solution. The main effect of the reflection potential is to cause all upward traveling electrons with kinetic energy below 20 eV at the top of the computational to be turned around and return toward the ionosphere. This causes two important effects. First, the net number flux should be decreased due to the increased number of downward traveling electrons. The net number flux from the superthermal electron solution,  $j_{se}$ , is given by

$$j_{se} = 2\pi \int_{E_{min}}^{E_{max}} \int_{-1}^1 \mu \phi(\mu, E) d\mu dE \tag{12}$$



where  $E$  is the kinetic energy,  $\mu$  is the cosine of the local pitch angle, and  $\phi(\mu, E)$  is the differential flux of superthermal electrons. Second, the energy deposition should be enhanced as electrons that would have previously escaped are now returned to the ionosphere where they have another opportunity to deposit energy. The energy deposition rate,  $Q_{se}$ , at a particular position along the magnetic field is given by [Liemohn *et al.*, 1997]:

$$Q_{se} = An_e \left[ \phi(E_{\min}) \left( 1 - \frac{2T_e}{E_{\min}} \right) + \int_{E_{\min}}^{E_{\max}} \frac{\phi(E)}{E} dE \right] \quad (13)$$

where  $A$  is a constant,  $n_e$  is the thermal electron density, and  $\phi(E)$  is the omnidirectional flux of superthermal electrons at a particular  $E$ . We note that this expression for the energy deposition rate does not include the effect of the so-called local heating resulting from the electron production. However, based on the work of Hoegy [1984], it is expected that this term would result in a relatively small correction.

Figure 12 shows both of these quantities. As most of the energy deposition happens in the ionosphere, we focus our plot on that part of the solution. Figure 12 (top) shows energy deposition, and Figure 12 (bottom) shows the net number flux. The case with reflection potential is shown as a solid line, and the case with no reflection potential is shown as a dashed line. As you can see the reflection potential only increases the energy deposition modestly. Integrating the energy deposition rate along the field line, we find that the total energy deposition with the inclusion of a reflection potential is only about 6% greater than when no reflection potential is included. In contrast, the effect on the number flux is more pronounced with the number flux at the top of the ionosphere decreased by a little less than half when the reflection potential is included. From this we conclude that the effect of the reflection potential is felt more strongly through the enforcement of the current conservation condition (equation (2)) than in any added heating.

Overall, we found that the presence of a high-altitude potential drop has only a slight effect on the overall solution. Nevertheless, how and where the potential drop forms, and what consequences it may have at high altitudes, and how it varies are interesting questions deserving of future study. In this work, however, we content ourselves with the demonstration that it has at best a marginal effect on our conclusions.

#### 4. Conclusion

We have presented a newly coupled model capable of treating superthermal electrons in the global polar wind solution. The STET model provides the solution for the superthermal electrons population, and the PWOM code provides the polar wind ion solution. The models interact through the ambipolar electric field, Coulomb collisions, and ionization (production of an SE must be paired with the production of an ion). The newly coupled model takes advantage of parallel computing in order to simultaneously obtain hundreds of field-aligned PWOM-STET solutions.

In this paper, we focused on the role of photoelectrons in the polar wind. We used the newly coupled PWOM-STET code to examine single stationary field lines under dayside and nightside conditions of illumination, as well as multiple moving field lines to reconstruct the effect of photoelectrons on the global polar wind solution. Finally, we examined the effect of an imposed reflection potential on our conclusions.

In summary we found the following:

1.  $O^+$  dominated the solution in our simulations below 4000 km on the dayside and 1800 km on the nightside. This corresponds to higher ion production and photoelectron fluxes on the dayside versus the nightside. We note, however, that the accuracy of the transition altitude will be strongly affected by the temperature at low altitudes. Future work is therefore needed to understand the qualitative difference between the electron and ion temperatures around 500 km in our calculation with the observations shown in Glocer *et al.* [2012].
2. Ion velocities show a clear day-night asymmetry with higher velocities on the dayside as compared to the nightside. This finding is in accordance with Akebono observation demonstrating that polar wind velocity is higher in the dayside high-latitude region than the nightside [Abe *et al.*, 1993].
3. Convection in the high-latitude region creates structure in the global polar wind solution. This is because the field line encounters changing conditions of illumination and different neutral thermosphere configurations as it moves. The electrons, owing to their light mass, respond much faster to these varying conditions as compared to ions. The different response rate results in localized enhanced ion temperatures along the tongue of ionization going into the nightside as the electrons cool more quickly than the ions. Likewise,

there are local patches of enhanced electron temperature where field lines move from night to day as the electrons heat up more quickly than the ions.

4. Including Joule heating, the frictional heating associated with the horizontal motion of the field line, results in localized ion temperature enhancements in regions of strong convection. There is also an associated increase in ion densities and the  $O^+$  to  $H^+$  ratio at higher altitudes. This is consistent with the results of Cannata *et al.* [1988] who also predicted such an increase using single field line simulations and imposed Joule heating rates.
5. The inclusion of a high-altitude reflection potential above the computational domain had only a slight effect on the overall solution.

In conclusion, we note that this work represents the first inclusion of a fully kinetic treatment of the superthermal electron population into the global polar wind solution. Our study focused primarily on the role of photoelectrons, and other processes such as auroral precipitation and wave-particle interactions are left to future studies.

### Acknowledgments

This work was funded by an award from the NASA Geospace Research Program. Resources supporting this work were provided by the NASA High-End Computing (HEC) Program through the NASA Advanced Supercomputing (NAS) Division at Ames Research Center. The model described in this paper has been included in the Space Weather Modeling Framework, which can be accessed online at <http://csem.engin.umich.edu/tools/swmf/downloads.php>. Model results are available upon request.

### References

- Abe, T., B. A. Whalen, A. W. Yau, S. Watanabe, E. Sagawa, and K. I. Oyama (1993), Altitude profile of the polar wind velocity and its relationship to ionospheric conditions, *Geophys. Res. Lett.*, *20*, 2825–2828, doi:10.1029/93GL02837.
- Abe, T., A. W. Yau, S. Watanabe, M. Yamada, and E. Sagawa (2004), Long-term variation of the polar wind velocity and its implication for the ion acceleration process: Akebono/suprathermal ion mass spectrometer observations, *J. Geophys. Res.*, *109*, A09305, doi:10.1029/2003JA010223.
- Axford, W. I. (1968), The polar wind and the terrestrial helium budget, *J. Geophys. Res.*, *73*, 6855–6859.
- Banks, P. M., and T. E. Holzer (1968), The polar wind, *J. Geophys. Res.*, *73*, 6846–6854, doi:10.1029/JA073i021p06846.
- Brinton, H. C., J. M. Grebowsky, and H. G. Mayr (1971), Altitude variation of ion composition in the midlatitude trough region: Evidence for upward plasma flow, *J. Geophys. Res.*, *76*, 3738–3745, doi:10.1029/JA076i016p03738.
- Cannata, R. W., T. L. Killeen, T. I. Gombosi, A. G. Burns, and R. G. Roble (1988), Modelling of time-dependent ion outflows at high geomagnetic latitudes, *Adv. Space Res.*, *8*, 89–92, doi:10.1016/0273-1177(88)90267-0.
- Chandler, M. O., T. E. Moore, and J. H. Waite Jr. (1991), Observations of polar ion outflows, *J. Geophys. Res.*, *96*, 1421–1428, doi:10.1029/90JA02180.
- Chappell, C. R., T. E. Moore, and J. H. Waite (1987), The ionosphere as a fully adequate source of plasma for the Earth's magnetosphere, *J. Geophys. Res.*, *92*, 5896–5910.
- Chiu, Y. T., and M. Schulz (1978), Self-consistent particle and parallel electrostatic field distributions in the magnetospheric-ionospheric auroral region, *J. Geophys. Res.*, *83*(A2), 629–642, doi:10.1029/JA083iA02p00629.
- Dessler, A. J., and F. C. Michel (1966), Plasma in the geomagnetic tail, *J. Geophys. Res.*, *71*(5), 1421–1426, doi:10.1029/JZ071i005p01421.
- Drob, D. P., et al. (2008), An empirical model of the Earth's horizontal wind fields: HWM07, *J. Geophys. Res.*, *113*, A12304, doi:10.1029/2008JA013668.
- Glocer, A., T. I. Gombosi, G. Toth, K. C. Hansen, A. J. Ridley, and A. Nagy (2007), Polar wind outflow model: Saturn results, *J. Geophys. Res.*, *112*, A01304, doi:10.1029/2006JA011755.
- Glocer, A., G. Toth, T. Gombosi, and D. Welling (2009a), Modeling ionospheric outflows and their impact on the magnetosphere, initial results, *J. Geophys. Res.*, *114*, A05216, doi:10.1029/2009JA014053.
- Glocer, A., G. Toth, Y. Ma, T. Gombosi, J.-C. Zhang, and L. M. Kistler (2009b), Multifluid block-adaptive-tree solar wind roe-type upwind scheme: Magnetospheric composition and dynamics during geomagnetic storms—Initial results, *J. Geophys. Res.*, *114*, A12203, doi:10.1029/2009JA014418.
- Glocer, A., N. Kitamura, G. Toth, and T. Gombosi (2012), Modeling solar zenith angle effects on the polar wind, *J. Geophys. Res.*, *117*, A04318, doi:10.1029/2011JA017136.
- Gombosi, T. I., and A. Nagy (1989), Time-dependent modeling of field aligned current-generated ion transients in the polar wind, *J. Geophys. Res.*, *94*, 359–369.
- Gombosi, T. I., T. E. Cravens, and A. F. Nagy (1985), A time-dependent theoretical model of the polar wind: Preliminary results, *Geophys. Res. Lett.*, *12*, 167–170.
- Hedin, A. (1983), A revised thermospheric model based on mass spectrometer and incoherent scatter data: MSIS-83, *J. Geophys. Res.*, *88*, 10,170–10,188.
- Hedin, A. (1987), MSIS-86 thermospheric model, *J. Geophys. Res.*, *92*, 4649–4662.
- Hedin, A. (1991), Extension of the MSIS thermosphere model into the middle and lower atmosphere, *J. Geophys. Res.*, *96*, 1159–1172.
- Hinteregger, H., K. Fukui, and B. Gibson (1981), Observational, reference and model data on solar EUV from measurements on AE-E, *Geophys. Res. Lett.*, *8*, 1147–1150.
- Hoegy, W. R. (1984), Thermal electron heating rate: A derivation, *J. Geophys. Res.*, *89*(A2), 977–985, doi:10.1029/JA089iA02p00977.
- Hoffman, J. H. (1970), Studies of the composition of the ionosphere with a magnetic deflection mass spectrometer, *Int. J. Mass Spectrom. Ion Phys.*, *4*, 315–322.
- Hoffman, J. H., W. H. Dodson, C. R. Lippincott, and H. D. Hammack (1974), Initial ion composition results from the Isis 2 satellite, *J. Geophys. Res.*, *79*, 4246–4251, doi:10.1029/JA079i028p04246.
- Khazanov, G., and M. W. Liemohn (1995), Nonsteady state ionosphere-plasmasphere coupling of superthermal electrons, *J. Geophys. Res.*, *100*, 9669–9681.
- Khazanov, G. V., T. Neubert, and G. D. Gefan (1994), Unified theory of ionosphere-plasmasphere transport of suprathermal electrons, *IEEE Trans. Plasma Sci.*, *22*, 187–198, doi:10.1109/27.279022.
- Khazanov, G. V., M. W. Liemohn, and T. E. Moore (1997), Photoelectron effects on the self-consistent potential in the collisionless polar wind, *J. Geophys. Res.*, *102*, 7509–7522, doi:10.1029/96JA03343.
- Khazanov, G. V., M. W. Liemohn, E. N. Krivorutsky, and T. E. Moore (1998), Generalized kinetic description of a plasma in an arbitrary field-aligned potential energy structure, *J. Geophys. Res.*, *103*, 6871–6890, doi:10.1029/97JA03436.

- Khazanov, G. V., A. Gloer, M. W. Liemohn, and E. W. Himwich (2013), Superthermal electron energy interchange in the ionosphere-plasmasphere system, *J. Geophys. Res. Space Physics*, *118*, 925–934, doi:10.1002/jgra.50127.
- Kitamura, N., Y. Ogawa, Y. Nishimura, N. Terada, T. Ono, A. Shinbori, A. Kumamoto, V. Truhlik, and J. Smilauer (2011), Solar zenith angle dependence of plasma density and temperature in the polar cap ionosphere and low-altitude magnetosphere during geomagnetically quiet periods at solar maximum, *J. Geophys. Res.*, *116*, A08227, doi:10.1029/2011JA016631.
- Kitamura, N., K. Seki, Y. Nishimura, N. Terada, T. Ono, T. Hori, and R. J. Strangeway (2012), Photoelectron flows in the polar wind during geomagnetically quiet periods, *J. Geophys. Res.*, *117*, A07214, doi:10.1029/2011JA017459.
- Kitamura, N., K. Seki, Y. Nishimura, and J. P. McFadden (2015), Limited impact of escaping photoelectrons on the terrestrial polar wind flux in the polar cap, *Geophys. Res. Lett.*, *42*, 3106–3113, doi:10.1002/2015GL063452.
- Knight, S. (1972), Parallel electric fields, *Planet. Space Sci.*, *21*, 741–750.
- Lee, J. S., J. P. Doering, T. A. Potemra, and L. H. Brace (1980), Measurements of the ambient photoelectron spectrum from atmosphere explorer: II. AE-E measurements from 300 to 1000 km during solar minimum conditions, *Planet. Space Sci.*, *28*, 973–996, doi:10.1016/0032-0633(80)90059-8.
- Lemaire, J. (1972), Effect of escaping photoelectrons in a polar exospheric model, *Space Res.*, *12*, 1413–1416.
- Lennartsson, W., R. D. Sharp, E. G. Shelley, R. G. Johnson, and H. Balsiger (1981), Ion composition and energy distribution during 10 magnetic storms, *J. Geophys. Res.*, *86*, 4628–4638, doi:10.1029/JA086iA06p04628.
- Liemohn, M. W., and G. V. Khazanov (1995), Nonsteady state coupling processes in superthermal electron transport, in *Cross-Scale Coupling in Space Plasmas*, *Geophys. Monogr. Ser.*, vol. 93, edited by J. L. Horwitz, N. Singh, and J. L. Burch, pp. 181–191, AGU, Washington, D. C.
- Liemohn, M. W., and G. V. Khazanov (1998), Collisionless plasma modeling in an arbitrary potential energy distribution, *Phys. Plasmas*, *5*(3), 580–589, doi:10.1063/1.872750.
- Liemohn, M. W., G. V. Khazanov, T. E. Moore, and S. M. Guiter (1997), Self-consistent superthermal electron effects on plasmaspheric refilling, *J. Geophys. Res.*, *102*, 7523–7536, doi:10.1029/96JA03962.
- Nishida, A. (1966), Formation of plasmopause, or magnetospheric plasma knee, by the combined action of magnetospheric convection and plasma escape from the tail, *J. Geophys. Res.*, *71*(23), 5669–5679, doi:10.1029/JZ071i023p05669.
- Peterson, W. K., T. N. Woods, P. C. Chamberlin, and P. G. Richards (2008), Photoelectron flux variations observed from the FAST satellite, *Adv. Space Res.*, *42*, 947–956, doi:10.1016/j.asr.2007.08.038.
- Richards, P. G., T. N. Woods, and W. K. Peterson (2006), Heuvac: A new high resolution solar EUV proxy model, *Adv. Space Res.*, *37*(2), 315–322, doi:10.1016/j.asr.2005.06.031. thermospheric-Ionospheric-Geospheric(TIGER)Symposium.
- Shay, M. A., J. F. Drake, M. Swisdak, and B. N. Rogers (2004), The scaling of embedded collisionless reconnection, *Phys. Plasmas*, *11*, 2199–2213, doi:10.1063/1.1705650.
- Shelley, E. G., R. G. Johnson, and R. D. Sharp (1972), Satellite observations of energetic heavy ions during a geomagnetic storm, *J. Geophys. Res.*, *77*, 6104–6110, doi:10.1029/JA077i031p06104.
- Solomon, S. C., S. M. Bailey, and T. N. Woods (2001), Effect of solar soft X-rays on the lower ionosphere, *Geophys. Res. Lett.*, *28*(11), 2149–2152, doi:10.1029/2001GL012866.
- Strobel, D. F., T. R. Young, R. R. Meier, T. P. Coffey, and A. W. Ali (1974), The nighttime ionosphere: *E* region and lower *F* region, *J. Geophys. Res.*, *79*, 3171–3178, doi:10.1029/JA079i022p03171.
- Su, Y.-J., J. L. Horwitz, G. R. Wilson, P. G. Richards, D. G. Brown, and C. W. Ho (1998), Self-consistent simulation of the photoelectron-driven polar wind from 120 km to 9  $R_E$  altitude, *J. Geophys. Res.*, *103*, 2279–2296, doi:10.1029/97JA03085.
- Tam, S. W. Y., F. Yasseen, T. Chang, and S. B. Ganguli (1995), Self-consistent kinetic photoelectron effects on the polar wind, *Geophys. Res. Lett.*, *22*, 2107–2110, doi:10.1029/95GL01846.
- Tam, S. W. Y., F. Yasseen, and T. Chang (1998), Further development in theory/data closure of the photoelectron-driven polar wind and day-night transition of the outflow, *Ann. Geophys.*, *16*, 948–968, doi:10.1007/s00585-998-0948-2.
- Titheridge, J. E. (2000), Modelling the peak of the ionospheric *E*-layer, *J. Atmos. Sol. Terr. Phys.*, *62*, 93–114, doi:10.1016/S1364-6826(99)00102-9.
- Varney, R. H., S. C. Solomon, and M. J. Nicolls (2014), Heating of the sunlit polar cap ionosphere by reflected photoelectrons, *J. Geophys. Res. Space Physics*, *119*, 8660–8684, doi:10.1002/2013JA019378.
- Weimer, D. R. (2005), Improved ionospheric electrodynamic models and application to calculating Joule heating rates, *J. Geophys. Res.*, *110*, A05306, doi:10.1029/2004JA010884.
- Welling, D. T., et al. (2016), The Earth: Plasma sources, losses, and transport processes, in *Plasma Sources of Solar System Magnetospheres*, edited by A. F. Nagy et al., pp. 145–208, Springer, New York, doi:10.1007/978-1-4939-3544-4\_5.
- Wilson, G. R., G. Khazanov, and J. L. Horwitz (1997), Achieving zero current for polar wind outflow on open flux tubes subjected to large photoelectron fluxes, *Geophys. Res. Lett.*, *24*, 1183–1186, doi:10.1029/97GL00923.
- Wilson, J. K., J. Baumgardner, and M. Mendillo (1998), Three tails of comet Hale-Bopp, *Geophys. Res. Lett.*, *25*, 225–228.
- Yau, A. W., B. A. Whalen, T. Abe, T. Mukai, K. I. Oyama, and T. Chang (1995), Akebono observations of electron temperature anisotropy in the polar wind, *J. Geophys. Res.*, *100*, 17,451–17,464, doi:10.1029/95JA00855.
- Yau, A. W., T. Abe, and W. K. Peterson (2007), The polar wind: Recent observations, *J. Atmos. Sol. Terr. Phys.*, *69*, 1936–1983, doi:10.1016/j.jastp.2007.08.010.